Automatica 163 (2024) 111556

Contents lists available at ScienceDirect

Automatica

journal homepage: www.elsevier.com/locate/automatica

Brief paper

A uniform semiglobal exponential stable adaptive line-of-sight (ALOS) guidance law for 3-D path following☆

Thor I. Fossen [a,*], A. Pedro Aguiar [b]

[a] Department of Engineering Cybernetics, Norwegian University of Science and Technology, Trondheim, Norway
[b] Department of Electrical and Computer Engineering, Faculty of Engineering, University of Porto, Porto, Portugal

ARTICLE INFO

Article history:
Received 12 November 2022
Received in revised form 23 October 2023
Accepted 6 January 2024
Available online xxxx

Keywords:
Guidance systems
Kinematics
Aircraft
Autonomous vehicles
Marine systems

ABSTRACT

This paper presents a 3-D adaptive line-of-sight (ALOS) path-following algorithm for autonomous vehicles, marine craft, and aircraft. The origins of the cross- and vertical-track errors are proven to be uniform semiglobal exponential stable (USGES). The stability proof is based on a kinematic amplitude-phase representation of the North-East-Down (NED) positional rates instead of the classical Euler angle rotation matrix representation. Parameter adaption is used to obtain integral action such that the vehicle converges to the path in the presence of winds, waves, and ocean currents. Typical applications are guidance and path-following control systems for autonomous vehicles, marine craft, and aircraft, where the horizontal- and vertical-plane motions are strongly coupled.

© 2024 The Author(s). Published by Elsevier Ltd. This is an open access article under the CC BY license (http://creativecommons.org/licenses/by/4.0/).

1. Introduction

Autonomous vehicles, marine craft, and aircraft can follow a path in 2-D and 3-D space by using line-of-sight (LOS) guidance laws to compute setpoints to the altitude/depth and heading/course autopilots; see Beard and McLain (2012), Breivik and Fossen (2005), Fossen (2021), Lekkas and Fossen (2013) and Yanushevsky (2011). The objective of a path-following controller is to follow a predefined path independent of time; that is, there are no temporal constraints. This means that no restrictions are placed on the temporal propagation along the path (Aguiar et al., 2008). The study in this article is limited to path-following control systems that can be implemented as interconnected systems. The advantage is that a conventional autopilot can be used in the inner control loop, while the LOS guidance law is implemented in the outer control loop.

1.1. 2-D LOS guidance laws for path following

Many vehicle control systems use proportional LOS guidance laws for path following, where the proportional gain is the inverse of the look-ahead distance. For 2-D path-following problems, the LOS guidance law can mimic the heading angle command of an experienced navigator (Healey & Lienard, 1993). Applications to marine craft are discussed by Breivik and Fossen (2009), Fossen et al. (2003) and Pettersen and Lefeber (2001). A similar approach has been applied to small uncrewed aerial vehicles (UAVs) by Nelson et al. (2007). This work uses a vector field surrounding the path generating course commands to guide the UAV towards the desired path. A comparative study of the LOS and vector-field guidance laws are found in Caharija et al. (2015). Proportional guidance laws also guide missiles; see Siouris (2010), and Yanushevsky (2011). Model-based predictive control (MPC) laws have been designed for LOS guidance by numerous authors; see Liu et al. (2015), Oh and Sun (2010), Pavlov et al. (2009) and Rout and Subudhi (2021). Uniform global asymptotic stability (UGAS) of the *proportional* LOS guidance law was first proven by Pettersen and Lefeber (2001). Later, Fossen and Pettersen (2014) have shown that the origin of the tracking error dynamics is USGES. This guarantees strong convergence and robustness properties to perturbations (Pettersen, 2017).

Despite the effectiveness and popularity of *proportional* LOS guidance laws, they have limitations when the vehicle is exposed to *drift forces* caused by winds, waves, and ocean currents. The consequence can be significant tracking errors during path following. The standard solution to this problem is integral LOS (ILOS); see Børhaug et al. (2008). The ILOS guidance law has been successfully implemented in many applications; see Caharija (2014) and Caharija et al. (2016). Extensions to path following for curved paths have been made by Lekkas and Fossen (2014).

☆ The work of A. P. Aguiar was partly supported by the project RELIABLE (PTDC/EEI-AUT/3522/2020) through the national funds FCT/MCTES, Portugal. The material in this paper was not presented at any conference. This paper was recommended for publication in revised form by Associate Editor Manfredi Maggiore under the direction of Editor Luca Zaccarian.

* Corresponding author.
E-mail addresses: thor.fossen@ntnu.no (T.I. Fossen), pedro.aguiar@fe.up.pt (A.P. Aguiar).

https://doi.org/10.1016/j.automatica.2024.111556
0005-1098/© 2024 The Author(s). Published by Elsevier Ltd. This is an open access article under the CC BY license (http://creativecommons.org/licenses/by/4.0/).

The integral state in the ILOS guidance law can also be replaced by a parameter for adaptive sideslip compensation (Fossen et al., 2015). Furthermore, Fossen and Lekkas (2015) have derived indirect and direct adaptive control laws for LOS path following. An alternative design method is the reduced-order extended state observer for estimation of the crab angle, known as the ELOS guidance law (Liu et al., 2017). A comparative study of the ALOS, ELOS, and ILOS guidance laws for 2-D path following is found in Fossen (2023a).

1.2. 3-D LOS guidance laws for path following

The horizontal-plane LOS guidance principle has been extended to 3-D path following by adding a second LOS guidance law for altitude/depth control by assuming that the motions between the horizontal and vertical planes are decoupled; see Caharija (2014) and Lekkas and Fossen (2013). This work assumes that the roll motions can be neglected in stability analysis. Several 3-D path-following algorithms have been compared for UAVs by Pelizer et al. (2017). This study concluded that the proportional LOS guidance law has smaller tracking errors for straight-line path following than the vector-field guidance law (Beard & McLain, 2012, Ch. 10) and the virtual target L_1-based guidance law (Park et al., 2007). Monte Carlo simulations have been used to analyze five 3-D path-following algorithms by Sujit et al. (2014), and robustness to wind loads and tuning are discussed in detail. However, the main limitation of the algorithms above is the lack of integral action to compensate for drift. In addition, the stability analysis is not valid for non-zero roll angles and couplings between the horizontal- and vertical-plane motions.

1.3. Main contributions

The paper's primary objective is 3-D *path following* specified by waypoints where the cross- and vertical-track errors are minimized for a moving vehicle without knowing the speed. The vehicle should converge to and follow a 3-D straight-line path without speed requirements and not synchronize to a virtual target (moving particle) along the path (Breivik & Fossen, 2005). A fundamental result of the paper is the ALOS guidance law for 3-D path following, which extends the 2-D results of Fossen (2023a). The guidance law is derived using a 3-D kinematic amplitude-phase representation of the NED differential equations (Fossen, 2023b). An essential theoretical contribution is the USGES stability proof, which guarantees that the origins of the cross- and vertical-track errors converge exponentially to zero. In addition, the stability analysis is valid for non-zero roll angles and coupled horizontal- and vertical-plane motions.

2. Kinematics

For marine craft and aircraft, the motion components in the BODY frame $\{b\}$ are defined as *surge, sway, heave, roll, pitch* and *yaw*. The NED reference frame is denoted by $\{n\}$. During path following a third reference frame $\{p\}$ transforming the NED frame to a frame with an axis parallel to the path is introduced; see Fig. 1. Consider a straight-line segment given by two waypoints (x_i^n, y_i^n, z_i^n) and $(x_{i+1}^n, y_{i+1}^n, z_{i+1}^n)$ expressed in $\{n\}$. Then the path-tangential coordinate system $\{p\}$ has its origin located at (x_i^n, y_i^n, z_i^n) and the x_p-axis is pointing towards the next waypoint $(x_{i+1}^n, y_{i+1}^n, z_{i+1}^n)$.

2.1. Along-, cross- and vertical-track errors

The *along-*, *cross-* and *vertical-track* errors (x_e^p, y_e^p, z_e^p) expressed in $\{p\}$ are given by the product of two basic rotation matrices, which rotate the NED tracking errors an *azimuth angle* π_h about the z axis and an *elevation angle* π_v about the resulting y axis from the first rotation. This is mathematically equivalent to

$$\begin{bmatrix} x_e^p \\ y_e^p \\ z_e^p \end{bmatrix} = \boldsymbol{R}_{y,\pi_v}^\top \boldsymbol{R}_{z,\pi_h}^\top \left(\begin{bmatrix} x^n \\ y^n \\ z^n \end{bmatrix} - \begin{bmatrix} x_i^n \\ y_i^n \\ z_i^n \end{bmatrix} \right) \tag{1}$$

where $\boldsymbol{p}^n = [x^n, y^n, z^n]^\top$ is the vehicle's position vector expressed in $\{n\}$. The rotation matrices are

$$\boldsymbol{R}_{y,\pi_v} = \begin{bmatrix} \mathrm{c}\pi_v & 0 & \mathrm{s}\pi_v \\ 0 & 1 & 0 \\ -\mathrm{s}\pi_v & 0 & \mathrm{c}\pi_v \end{bmatrix} \boldsymbol{R}_{z,\pi_h} = \begin{bmatrix} \mathrm{c}\pi_h & -\mathrm{s}\pi_h & 0 \\ \mathrm{s}\pi_h & \mathrm{c}\pi_h & 0 \\ 0 & 0 & 1 \end{bmatrix} \tag{2}$$

where $\mathrm{s}\cdot = \sin(\cdot)$ and $\mathrm{c}\cdot = \cos(\cdot)$, and

$$\pi_h = \mathrm{atan2}(y_{i+1}^n - y_i^n, x_{i+1}^n - x_i^n) \tag{3}$$

$$\pi_v = \mathrm{atan2}\left(-(z_{i+1}^n - z_i^n), \sqrt{(x_{i+1}^n - x_i^n)^2 + (y_{i+1}^n - y_i^n)^2}\right) \tag{4}$$

2.2. NED kinematic differential equations

Let $\boldsymbol{v}^b = [u, v, w]^\top$ be the vehicle's linear velocity vector expressed in $\{b\}$. Consequently, the kinematic differential equation is (Fossen, 2021, Ch. 2)

$$\dot{\boldsymbol{p}}^n = \boldsymbol{R}_b^n \boldsymbol{v}^b \tag{5}$$

where $\boldsymbol{R}_b^n$ is the Euler angle rotation matrix (*zyx* convention)

$$\boldsymbol{R}_b^n = \begin{bmatrix} \mathrm{c}\psi\mathrm{c}\theta & -\mathrm{s}\psi\mathrm{c}\phi + \mathrm{c}\psi\mathrm{s}\theta\mathrm{s}\phi & \mathrm{s}\psi\mathrm{s}\phi + \mathrm{c}\psi\mathrm{c}\phi\mathrm{s}\theta \\ \mathrm{s}\psi\mathrm{c}\theta & \mathrm{c}\psi\mathrm{c}\phi + \mathrm{s}\phi\mathrm{s}\theta\mathrm{s}\psi & -\mathrm{c}\psi\mathrm{s}\phi + \mathrm{s}\theta\mathrm{s}\psi\mathrm{c}\phi \\ -\mathrm{s}\theta & \mathrm{c}\theta\mathrm{s}\phi & \mathrm{c}\theta\mathrm{c}\phi \end{bmatrix} \tag{6}$$

2.3. Amplitude-phase form of the NED kinematic differential equations

When analyzing the stability properties of the ALOS guidance law in Section 4, a 3-D amplitude-phase representation of the kinematic differential equation (5) will be used. Proposition 1 summarizes the kinematic model.

Proposition 1 (*3-D Amplitude-Phase Form*)**.** *For a vehicle with surge velocity* $0 < u_{min} \leq u \leq u_{\max}$*, the kinematic differential equation* (5) *for the NED positional rates can be expressed by*

$$\dot{x}^n = U_h \cos(\psi + \beta_c) \tag{7}$$

$$\dot{y}^n = U_h \sin(\psi + \beta_c) \tag{8}$$

$$\dot{z}^n = -U_v \sin(\theta - \alpha_c) \tag{9}$$

where the phase angles are

$$\alpha_c = \tan^{-1}\left(\frac{v\sin(\phi) + w\cos(\phi)}{u}\right) \tag{10}$$

$$\beta_c = \tan^{-1}\left(\frac{v\cos(\phi) - w\sin(\phi)}{U_v\cos(\theta - \alpha_c)}\right) \tag{11}$$

and the amplitudes U_h *and* U_v *are the horizontal and the vertical speed components, respectively, given by*

$$U_v = u\sqrt{1 + \tan^2(\alpha_c)} \tag{12}$$

$$U_h = U_v\cos(\theta - \alpha_c)\sqrt{1 + \tan^2(\beta_c)} \tag{13}$$

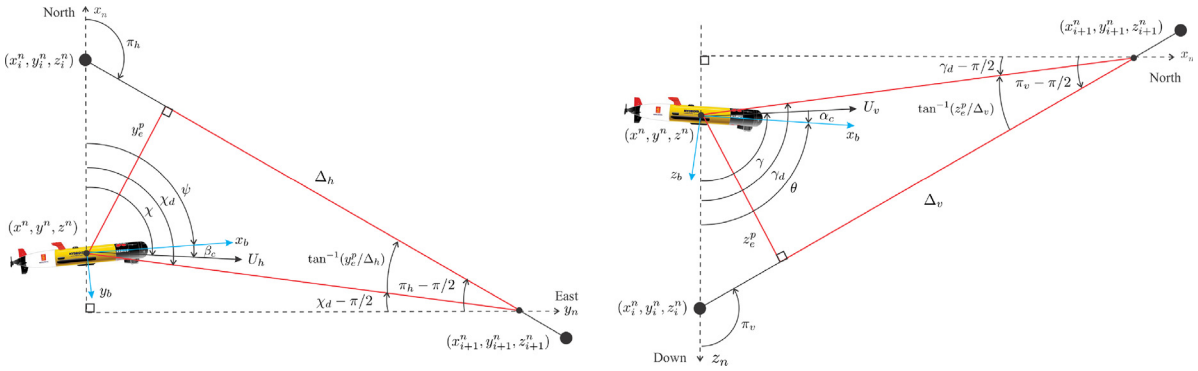

Fig. 1. LOS guidance geometry. The desired heading and pitch angles, $\psi_d = \chi_d - \beta_c = \pi_h - \beta_c - \tan^{-1}(y_e^p/\Delta_h)$ and $\theta_d = \gamma_d + \alpha_c = \pi_v + \alpha_c + \tan^{-1}(z_e^p/\Delta_v)$, are determined such that the vehicle speeds U_h and U_v are directed towards a point on the path specified by the look-ahead distances Δ_h and Δ_v.

Proof. See Fossen (2023b).

Note that under the influence of the environment, i.e., winds for aircraft, or winds, waves, and ocean currents for marine craft, the velocity vector $\boldsymbol{v}^b$ will be changed by the environmental forces. If the linear velocities u, v, and w change, α_c and β_c given by (10) and (11) change. The environmental disturbances can be simulated using the concept of the relative velocity vector, which is the difference between the vehicle velocity $\boldsymbol{v}^b$ and the flow velocity vectors (Fossen, 2021). During straight-line path following the following assumption will be made:

Assumption 1. The angles α_c and β_c are constant during path following such that $\dot{\alpha}_c = 0$ and $\dot{\beta}_c = 0$.

This is true for straight-line path following of vehicles moving at a constant speed. However, in practice, Assumption 1 can be relaxed to *nearly constant* to accommodate situations where the speed varies slowly due to time-varying environmental disturbances.

Remark 1. For zero roll, $\phi \equiv 0$, (10)–(11) reduce to

$$\alpha_c = \tan^{-1}\left(\frac{w}{u}\right) \tag{14}$$

$$\beta_c = \tan^{-1}\left(\frac{v}{U_v \cos(\theta - \alpha_c)}\right) \overset{\theta=0}{=} \tan^{-1}\left(\frac{v}{u}\right) \tag{15}$$

since $\cos(-\alpha_c) = \cos(-\tan^{-1}(w/u)) = u/U_v$ where $U_v = (u^2 + w^2)^{1/2}$. The decoupled horizontal-plane model for aircraft (Beard & McLain, 2012, Ch. 2.4), and marine craft (Fossen, 2021, Ch. 2.5) are obtained by expressing (7)–(8) as

$$\dot{x}^n = U_h \cos(\chi), \qquad \dot{y}^n = U_h \sin(\chi) \tag{16}$$

where $\chi := \psi + \beta_c$ is the course over ground (COG) and $U_h = (u^2 + v^2)^{1/2}$ is the speed over ground (SOG). The phase angle β_c is recognized as the *crab angle*. For the vertical plane (9) reduces to, $\dot{z}^n = -U_v \sin(\gamma)$, where $\gamma := \theta - \alpha_c$ is the *flight-path angle*.

2.4. Differential equations for the along-, cross- and vertical-track errors

The tracking-error dynamics expressed in $\{p\}$ is found by time differentiation of (1) and substitution of (7)–(9). This is mathematically equivalent to

$$\begin{bmatrix} \dot{x}_e^p \\ \dot{y}_e^p \\ \dot{z}_e^p \end{bmatrix} = \boldsymbol{R}_{y,\pi_v}^\top \boldsymbol{R}_{z,\pi_h}^\top \begin{bmatrix} U_h \cos(\psi + \beta_c) \\ U_h \sin(\psi + \beta_c) \\ -U_v \sin(\theta - \alpha_c) \end{bmatrix} \tag{17}$$

Expanding the last two rows of (17) corresponding to the cross- and vertical-track errors, yields

$$\dot{y}_e^p = U_h \sin(\psi + \beta_c - \pi_h) \tag{18}$$

$$\dot{z}_e^p = U_h \sin(\pi_v) \cos(\psi + \beta_c - \pi_h) - U_v \cos(\pi_v) \sin(\theta - \alpha_c) \tag{19}$$

For control design, it is advantageous to express the vertical-track differential equation (19) as a function of the term $\sin(\theta - \alpha_c - \pi_v)$. Substituting (13) into (19) yields

$$\begin{aligned} \dot{z}_e^p = {} & U_v \cos(\theta - \alpha_c)\sqrt{1 + \tan^2(\beta_c)} \sin(\pi_v) \cos(\psi + \beta_c - \pi_h) \\ & - U_v \cos(\pi_v) \sin(\theta - \alpha_c) \end{aligned} \tag{20}$$

Application of the trigonometric identity for the difference of two angles, $\sin(\theta - \alpha_c - \pi_v) = \sin(\theta - \alpha_c)\cos(\pi_v) - \cos(\theta - \alpha_c)\sin(\pi_v)$, to (20) gives

$$\begin{aligned} \dot{z}_e^p = {} & U_v \sin(\pi_v) \cos(\theta - \alpha_c)\sqrt{1 + \tan^2(\beta_c)} \cos(\psi + \beta_c - \pi_h) \\ & - U_v \sin(\pi_h) \cos(\theta - \alpha_c) - U_v \sin(\theta - \alpha_c - \pi_v) \\ = {} & -U_v \sin(\theta - \alpha_c - \pi_v) \\ & + U_v \sin(\pi_v) \cos(\theta - \alpha_c) \\ & \cdot \left(\sqrt{1 + \tan^2(\beta_c)} \cos(\psi + \beta_c - \pi_h) - 1\right) \end{aligned} \tag{21}$$

Finally, substituting (13) into (21) yields

$$\begin{aligned} \dot{z}_e^p = {} & -U_v \sin(\theta - \alpha_c - \pi_v) + \frac{U_h \sin(\pi_v)}{\sqrt{1 + \tan^2(\beta_c)}} \\ & \cdot \left(\sqrt{1 + \tan^2(\beta_c)} \cos(\psi + \beta_c - \pi_h) - 1\right) \end{aligned} \tag{22}$$

3. Conventional LOS guidance laws

To better grasp the proposed guidance law, this section briefly reviews the conventional methods for proportional LOS guidance.

3.1. Proportional LOS guidance laws

For fixed-wing aircraft, it is common to control the course angle χ. The desired course angle χ_d can be computed using the *vector-field guidance law* (Beard & McLain, 2012, Ch. 10)

$$\chi_d = \pi_h - \chi^\infty \frac{2}{\pi} \tan^{-1}\left(\frac{y_e^p}{\Delta_h}\right) \tag{23}$$

where $\Delta_h > 0$ is the user specified look-ahead distance and $\chi^\infty \in (0, \pi/2]$ defines the path approach angle when starting

far away. Note that the slope π_h of the desired path is given by (3). Eq. (18) with $\chi = \psi + \beta_c$ gives

$$\dot{y}_e^p = U_h \sin(\chi - \pi_h) \tag{24}$$

Assume that the course autopilot achieves perfect tracking such that $\chi = \chi_d$. Then

$$\dot{y}_e^p = U_h \sin\left(-\chi^\infty \frac{2}{\pi} \tan^{-1}\left(\frac{y_e^p}{\Delta_h}\right)\right) \tag{25}$$

If $\chi^\infty \in (0, \pi/2]$, the origin $y_e^p = 0$ can be shown to be uniformly globally asymptotically stable (UGAS) by using Lyapunov's direct method (Nelson et al., 2007). Also note that the vector-field guidance law (23) is equivalent to the classical *proportional LOS guidance law*

$$\chi_d = \pi_h - \tan^{-1}\left(\frac{y_e^p}{\Delta_h}\right) \tag{26}$$

if $\chi^\infty = \pi/2$. For this case, we can use $\sin(\tan^{-1}(x/d)) = x/\sqrt{d^2 + x^2}$ to obtain the cross-track error

$$\dot{y}_e^p = -\frac{U_h}{\sqrt{\Delta_h^2 + (y_e^p)^2}} y_e^p \tag{27}$$

Consequently, Lyapunov stability theory guarantees that the equilibrium point $y_e^p = 0$ of (27) is USGES (Fossen & Pettersen, 2014). The concept of a virtual target can also be used to guarantee that the aircraft follows the path: see Breivik and Fossen (2005) and Park et al. (2007). A clear distinction between LOS guidance and the L_1 controller developed by Park et al. (2007) is that the LOS look-ahead distance ahead of the vehicle is along the path. In contrast, the L_1 distance is the radius around the vehicle. Hence, the reference point is the intersection of this circle and the desired path. This resembles *enclosure-based* LOS (Fossen, 2021, Ch. 12.4).

Marine craft, however, can operate at very low speeds U_h. In such cases, neither the course angle χ nor the crab angle β_c will be well defined and unsuited for feedback control. This is why marine craft use heading autopilots to control the yaw angle ψ instead of χ. If a heading command (Healey & Lienard, 1993 Fossen, 2021, Ch. 12.5)

$$\psi_d = \pi_h - \beta_c - \tan^{-1}\left(\frac{y_e^p}{\Delta_h}\right) \tag{28}$$

is applied to (18) under the assumption that the heading autopilot achieves perfect tracking $\psi = \psi_d$, we obtain the error dynamics (27). Unfortunately, formula (28) requires knowledge of the crab angle β_c, which depends on the environment. Similarly, the angle α_c must be known when applying the proportional LOS guidance law to altitude or depth control. ILOS is the standard technique to compensate for the unknown angles α_c and β_c.

3.2. ILOS guidance laws

ILOS can be used to cancel drift (sideslip due to β_c) in the horizontal plane; see Børhaug et al. (2008), Caharija et al. (2016, 2015), Fossen and Lekkas (2015), Fossen et al. (2015) and Lekkas and Fossen (2014). This is based on the assumption that β_c is nearly constant. Caharija (2014) and Lekkas and Fossen (2013) have proposed extensions to the vertical plane under the assumption that the motions between the horizontal and vertical planes are decoupled and that the roll-induced motions can be neglected. The next section presents a novel adaptive LOS guidance law for coupled horizontal- and vertical-plane motions and compensation of the unknown angles α_c and β_c.

4. ALOS guidance law for 3-D path following

The main result of the paper is the ALOS guidance law

$$\boxed{\begin{aligned} \psi_d &= \pi_h - \hat{\beta}_c - \tan^{-1}\left(\frac{y_e^p}{\Delta_h}\right) && (29)\\ \dot{\hat{\beta}}_c &= \gamma_h \frac{\Delta_h}{\sqrt{\Delta_h^2 + (y_e^p)^2}} y_e^p && (30)\\ \theta_d &= \pi_v + \hat{\alpha}_c + \tan^{-1}\left(\frac{z_e^p}{\Delta_v}\right) && (31)\\ \dot{\hat{\alpha}}_c &= \gamma_v \frac{\Delta_v}{\sqrt{\Delta_v^2 + (z_e^p)^2}} z_e^p && (32) \end{aligned}}$$

for coupled horizontal- and vertical-plane motions governed by (18) and (22). Here, $\Delta_h > 0$ and $\Delta_v > 0$ are the user specified look-ahead distances, $\gamma_h > 0$ and $\gamma_v > 0$ are the adaptive gains, and $\hat{\beta}_c$ and $\hat{\alpha}_c$ are the parameter estimates of β_c and α_c, respectively. The stability analysis assumes that the heading and altitude/depth autopilots achieve perfect tracking such that $\psi = \psi_d$ and $\theta = \theta_d$. The ALOS guidance law can be robustified by using the parameter projections

$$\boxed{\begin{aligned} \dot{\hat{\beta}}_c &= \gamma_h \frac{\Delta_h}{\sqrt{\Delta_h^2 + (y_e^p)^2}} \mathrm{Proj}(\hat{\beta}_c, y_e^p) && (33)\\ \dot{\hat{\alpha}}_c &= \gamma_v \frac{\Delta_v}{\sqrt{\Delta_v^2 + (z_e^p)^2}} \mathrm{Proj}(\hat{\alpha}_c, z_e^p) && (34) \end{aligned}}$$

instead of (30) and (32). This restricts the parameter estimates to a compact set $|\hat{\beta}_c| \leq M_{\hat{\theta}}$ and $|\hat{\alpha}_c| \leq M_{\hat{\theta}}$ where $M_{\hat{\theta}} = M_\theta + \epsilon$, and $\epsilon > 0$ is a positive constant chosen such that $M_{\hat{\theta}}$ is slighter larger than M_θ where $|\beta_c| \leq M_\theta$ and $|\alpha_c| \leq M_\theta$. Furthermore,

$$\mathrm{Proj}(\hat{\theta}, \tau) = \begin{cases} \left(1 - c(\hat{\theta})\right)\tau & \text{if } |\hat{\theta}| > M_\theta \text{ and } \hat{\theta}^\top \tau > 0 \\ \tau & \text{otherwise} \end{cases} \tag{35}$$

where $c(\hat{\theta}) = \min\{1, (\hat{\theta}^2 - M_\theta^2)/(M_{\hat{\theta}}^2 - M_\theta^2)\}$ is a special case of the parameter projection algorithm by Krstic et al. (1995, Appendix E). As shown in Appendix A, the projection modifications (33)–(34) ensure semiglobal stability properties. Inserting (29) and (31) into (18) and (22), yields

$$\dot{y}_e^p = U_h \sin\left(\tilde{\beta}_c - \tan^{-1}\left(\frac{y_e^p}{\Delta_h}\right)\right) \tag{36}$$

$$\dot{z}_e^p = U_v \sin\left(\tilde{\alpha}_c - \tan^{-1}\left(\frac{z_e^p}{\Delta_v}\right)\right) + g(t, y_e^p, \tilde{\beta}_c) \tag{37}$$

where $\tilde{\alpha}_c = \alpha_c - \hat{\alpha}_c$, $\tilde{\beta}_c = \beta_c - \hat{\beta}_c$ and

$$g(t, y_e^p, \tilde{\beta}_c) = \frac{U_h \sin(\pi_v)}{\sqrt{1 + \tan^2(\beta_c)}} \cdot \left(\sqrt{1 + \tan^2(\beta_c)} \cos\left(\tilde{\beta}_c - \tan^{-1}\left(\frac{y_e^p}{\Delta_h}\right)\right) - 1\right) \tag{38}$$

Application of $\sin(a-b) = \sin(a)\cos(b) - \cos(a)\sin(b)$ to (36)–(37) gives

$$\begin{aligned} \dot{y}_e^p &= -U_h \sin\left(\tan^{-1}\left(\frac{y_e^p}{\Delta_h}\right)\right)\cos(\tilde{\beta}_c) \\ &\quad + U_h \cos\left(\tan^{-1}\left(\frac{y_e^p}{\Delta_h}\right)\right)\sin(\tilde{\beta}_c) \\ \dot{z}_e^p &= -U_v \sin\left(\tan^{-1}\left(\frac{z_e^p}{\Delta_v}\right)\right)\cos(\tilde{\alpha}_c) \end{aligned} \tag{39}$$

$$+ U_v \cos\left(\tan^{-1}\left(\frac{z_e^p}{\Delta_v}\right)\right)\sin(\tilde{\alpha}_c)$$
$$+ g(t, y_e^p, \tilde{\beta}_c) \tag{40}$$

Application of, $\sin(\tan^{-1}(x/d)) = x/\sqrt{d^2+x^2}$ and $\cos(\tan^{-1}(x/d)) = d/\sqrt{d^2+x^2}$, to (39)–(40) yields the nonlinear cascaded system

$$\Sigma_1 : \begin{cases} \dot{z}_e^p &= -\frac{U_v \Delta_v}{\sqrt{\Delta_v^2+(z_e^p)^2}}\left(\cos(\tilde{\alpha}_c)\frac{z_e^p}{\Delta_v} - \sin(\tilde{\alpha}_c)\right) \\ &\quad + g(t, y_e^p, \tilde{\beta}_c) \\ \dot{\hat{\alpha}}_c &= -\gamma_v \frac{\Delta_v}{\sqrt{\Delta_v^2+(z_e^p)^2}}\text{Proj}(\hat{\alpha}_c, z_e^p) \end{cases} \tag{41}$$

$$\Sigma_2 : \begin{cases} \dot{y}_e^p &= -\frac{U_h \Delta_h}{\sqrt{\Delta_h^2+(y_e^p)^2}}\left(\cos(\tilde{\beta}_c)\frac{y_e^p}{\Delta_h} - \sin(\tilde{\beta}_c)\right) \\ \dot{\hat{\beta}}_c &= -\gamma_h \frac{\Delta_h}{\sqrt{\Delta_h^2+(y_e^p)^2}}\text{Proj}(\hat{\beta}_c, y_e^p) \end{cases} \tag{42}$$

Note that $\dot{\tilde{\alpha}}_c = -\dot{\hat{\alpha}}_c$ and $\dot{\tilde{\beta}}_c = -\dot{\hat{\beta}}_c$ follow from Assumption 1. The Σ_1 and Σ_2 subsystems are nonautonomous systems since U_h, U_v and $g(t, y_e^p, \tilde{\beta}_c)$ vary with time. In some cases, it is advantageous to let the look-ahead distances Δ_h and Δ_v vary with time as well, e.g., by using optimization techniques (Pavlov et al., 2009) or the explicit formula by Lekkas and Fossen (2012).

The main stability results for the cascade Σ_1–Σ_2 are summarized by Lemmas 1–2 and Theorem 1, which assumes that Assumption 1 holds.

Lemma 1. *The origin $(z_e^p,\ \tilde{\alpha}_c) = (0,\ 0)$ of the Σ_1 subsystem is USGES if the perturbation $g(t, y_e^p, \tilde{\beta}_c) \equiv 0$.*

Proof. See Appendix A.

Lemma 2. *The origin $(y_e^p,\ \tilde{\beta}_c) = (0,\ 0)$ of the Σ_2 subsystem is USGES.*

Proof. See Appendix B.

Theorem 1. *Let the altitude/depth and heading autopilots guarantee that $\theta = \theta_d$ and $\psi = \psi_d$, and u is kept constant by the speed autopilot. Then, the ALOS guidance laws (29) and (31) with parameter update laws (33)–(34), applied to the cross- and vertical-track errors (18) and (22) with adaptive gains $\gamma_h > 0$ and $\gamma_v > 0$, render the origins $(y_e^p,\ \tilde{\beta}_c) = (0,\ 0)$ and $(z_e^p,\ \tilde{\alpha}_c - \tilde{\alpha}_c^{ss}) = (0,\ 0)$ of the cascade Σ_1–Σ_2 USGES. Here $\tilde{\alpha}_c^{ss}$ is a (small) constant steady-state value of $\tilde{\alpha}_c$, which vanishes for $\pi_v = 0$ (constant depth) or $\beta_c = 0$ (zero sideslip).*

Proof. See Appendix C.

Remark 2. The projection mechanism included in (33)–(34) enables us to show USGES, a property that implies robustness against unmodeled dynamics and exogenous bounded disturbances. From a practical point of view, it is observed that for most vehicles, the use of (30) and (32) instead of (33)–(34) still exhibit excellent path following, but in this case, there are no formal guarantees.

5. Case study with the Remus 100 AUV

The 6-DOF mathematical model of the Remus 100 AUV is available in the MATLAB MSS toolbox (Fossen & Perez, 2004). The script *remus100.m* describes an AUV of length 1.6 m, diameter of 19 cm and mass 31.9 kg (Fig. 2). The vehicle's maximum speed, 2.5 m/s, is obtained by running the propeller at 1525 rpm when there are no ocean currents. Depth is controlled by using the stern plane δ_s, while the tail rudder δ_r controls the yaw angle. The heading and depth autopilots are implemented as PID controllers

Fig. 2. The Remus 100 at the Applied Underwater Robotics Laboratory (AUR-Lab) at NTNU.

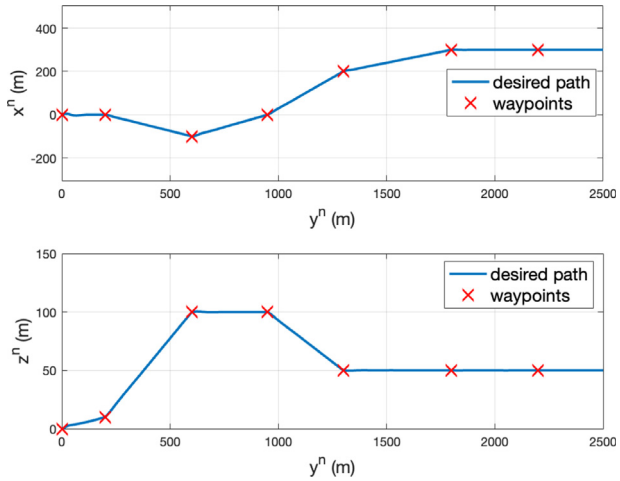

Fig. 3. Desired path and waypoints in the horizontal and vertical planes. The maximum depth of the vehicle is 100 m.

$$\delta_s = -k_{p_\theta}\,\text{ssa}(\tilde{\theta}) - k_{d_\theta}\dot{\theta} - k_{i_\theta}\int_0^t \text{ssa}(\tilde{\theta})\text{d}\tau \tag{43}$$

$$\delta_r = -k_{p_\psi}\,\text{ssa}(\tilde{\psi}) - k_{d_\psi}\dot{\psi} - k_{i_\psi}\int_0^t \text{ssa}(\tilde{\psi})\text{d}\tau \tag{44}$$

where $\tilde{\theta} = \theta - \theta_d$, $\tilde{\psi} = \psi - \psi_d$ and $\text{ssa}(\cdot)$ is the *smallest-signed angle* confining the argument to the interval $[-\pi, \pi)$. The controller gains were chosen as $k_{p_\theta} = 2.0$, $k_{d_\theta} = 3.0$, $k_{i_\theta} = 0.1$, $k_{p_\psi} = 4.8$, $k_{d_\psi} = 12.0$ and $k_{i_\psi} = 0.38$. The vehicle speed was not controlled. Instead, the propeller revolutions were initialized at 1000 rpm and increased to 1300 rpm. This increased the vehicle's initial speed from 1.0 m/s to a cruise speed just below 2.0 m/s (Fig. 5).

The ALOS guidance laws (29) and (31) with parameter update laws (33)–(34) were implemented using $\Delta_v = \Delta_h = 20$ m and $\gamma_v = \gamma_h = 0.002$. The sampling time was chosen as 20 Hz. The desired pitch and yaw angles and their true values are shown in Fig. 4, confirming that $\psi \approx \psi_d$ and $\theta \approx \theta_d$. The corresponding waypoints are shown in Fig. 3. Switching between the waypoints is important when implementing straight-line path following control systems. The next waypoint $(x_{i+1}^n, y_{i+1}^n, z_{i+1}^n)$ is selected based on whether or not the vehicle lies within a sphere of acceptance with radius R around $(x_{i+1}^n, y_{i+1}^n, z_{i+1}^n)$. The ocean current in the horizontal plane was initialized at 0.5 m/s with direction 150 degrees (Fig. 5), while the vertical component was chosen as 0.1 m/s. After 500 s the current direction was changed from 150 to 160 degrees using a Gauss–Markov process. Finally, the current speed was increased from 0.5 m/s to 0.65 m/s at time $t = 800$ s.

The parameter estimates $\hat{\alpha}_c$ and $\hat{\beta}_c$ track the true parameters α_c and β_c with excellent accuracy, also when the current speed

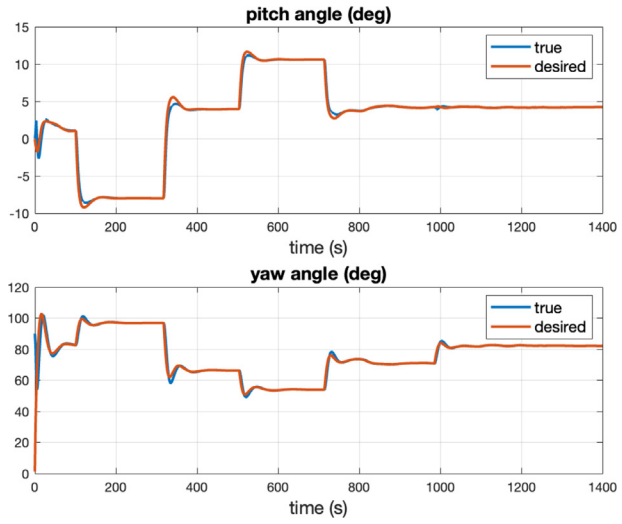

Fig. 4. ALOS desired pitch angle θ_d and yaw angle ψ_d together with their true values obtained by using the depth and heading autopilots.

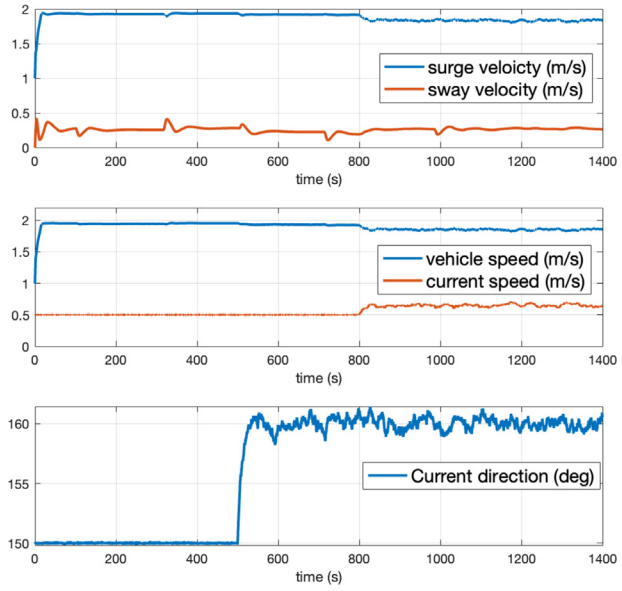

Fig. 5. Vehicle surge and sway velocities, speed and ocean current speed/direction in the horizontal plane versus time.

and direction change rapidly (Fig. 6). Note the angle of attack α and β are different from α_c and β_c, and that the vehicle will sideslip with an angle $\beta_c \approx 8.0$ degrees after 1400 s. The accuracy of the ALOS guidance law is demonstrated in Fig. 6 where y_e^p and z_e^p converge to zero. The initial transient is caused by a 90 degrees initial heading error, while the jumps in the tracking errors are due to waypoint switching.

6. Conclusions

This paper has presented a 3-D adaptive line-of-sight (ALOS) guidance law for path following inspired by the proportional line-of-sight (LOS) guidance laws used by ancient navigators.

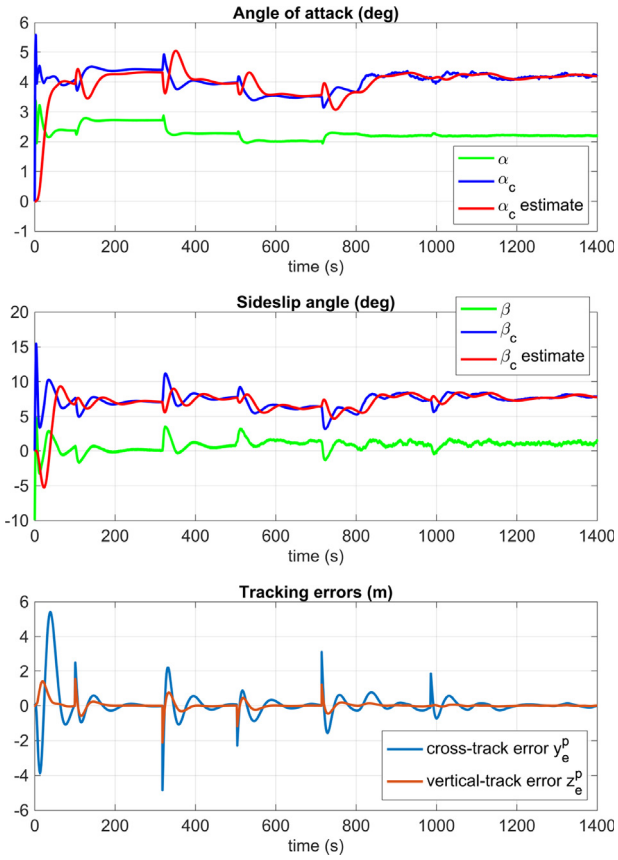

Fig. 6. The vertical-plane angles α, α_c and $\hat{\alpha}_c$, the horizontal-plane angles β, β_c and $\hat{\beta}_c$ and cross-track/vertical-track errors versus time.

The ALOS guidance law performed excellently during depth- and heading-changing maneuvers when the vehicle was exposed to a stochastic ocean current. Parameter adaption successfully removed offsets caused by the environment. The origins of the cross- and vertical-track errors were proven uniform semiglobal exponential stable (USGES). This extends previous results for 3-D LOS path following where the horizontal- and vertical-plane motions are assumed to be decoupled. The assumption that the roll motions are zero, such that a reduced-order model could be used in the stability analysis, was also removed. Instead, a 3-D amplitude-phase representation of the differential equations for North-East-Down positional rates was used to analyze the stability of the cross- and vertical-track errors. The motivation for this was to avoid the classical Euler angle rotation matrix representation, which complicates the stability analysis. Typical applications are autonomous vehicles, marine craft, and aircraft motion control systems for path following. Computer simulations using a high-fidelity model of an autonomous underwater vehicle confirm the theoretical results.

Appendix A. Proof of Lemma 1

The vertical-plane error dynamics (41) without perturbation, $g(t, y_e^p, \tilde{\beta}_c) \equiv 0$, can be expressed by

$$\dot{\boldsymbol{z}} = U_v \, \Omega_v(\boldsymbol{z}) \, (\boldsymbol{A}_v \boldsymbol{z} + \boldsymbol{d}_v(t, \boldsymbol{z})) \tag{A.1}$$

where $\boldsymbol{z} = [z_1, \, z_2]^\top := [z_e^p, \, \tilde{\alpha}_c]^\top$, and

$$\boldsymbol{A}_v = \begin{bmatrix} -\frac{1}{\Delta_v} & 1 \\ -\kappa_v & 0 \end{bmatrix}, \quad \Omega_v(\boldsymbol{z}) = \frac{\Delta_v}{\sqrt{\Delta_v^2 + (z_e^p)^2}} \tag{A.2}$$

where the speed U_v given by (12) is time varying and lower bounded by $0 < U_v^{\min} \leq U_v$, $\kappa_v = \gamma_v / U_v^{\min} > 0$, $\Delta_v > 0$, and

$$\boldsymbol{d}_v(t,\boldsymbol{z}) = \begin{bmatrix} \frac{1}{\Delta_v}(1-\cos(\tilde{\alpha}_c))\, z_e^p + \sin(\tilde{\alpha}_c) - \tilde{\alpha}_c \\ \kappa_v \left(z_e^p - \frac{U_v^{\min}}{U_v} \mathrm{Proj}\left(\hat{\alpha}_c, z_e^p\right)\right) \end{bmatrix} = \bar{\boldsymbol{d}}_v(t,\boldsymbol{z}) + \kappa_v \frac{U_v^{\min}}{U_v} \begin{bmatrix} 0 \\ Q \end{bmatrix} \tag{A.3}$$

where $0 < (U_v^{\min}/U_v) \leq 1$ and

$$\bar{\boldsymbol{d}}(t,\boldsymbol{z}) = \begin{bmatrix} \frac{1}{\Delta_v}(1-\cos(\tilde{\alpha}_c))\, z_e^p + \sin(\tilde{\alpha}_c) - \tilde{\alpha}_c \\ \kappa_v \left(1 - \frac{U_v^{\min}}{U_v}\right) z_e^p \end{bmatrix} \tag{A.4}$$

$$Q = \begin{cases} c(\hat{\alpha}_c) z_e^p & \text{if } |\hat{\alpha}_c| > M_\theta \text{ and } \hat{\alpha}_c^{\top} z_e^p > 0 \\ 0 & \text{otherwise} \end{cases} \tag{A.5}$$

Note that the adaptive law (34) has the same form as the one without projection (32) except for the additional term Q. Because of the convex property of the projection algorithm, we have that $Q\tilde{\alpha}_c \leq 0$ (Ioannou & Sun, 2012, Theorem 4.1.1). Therefore, the term $Q\tilde{\alpha}_c$ introduced by projection can only make the time derivative $\dot{V}$ of the Lyapunov function (to be introduced in the sequel) more negative. In addition, the perturbation term $\bar{\boldsymbol{d}}(t,\boldsymbol{z}) = [\bar{d}_1(t,\boldsymbol{z}), \bar{d}_2(t,\boldsymbol{z})]^{\top}$ satisfies

$$|\bar{d}_1(t,\boldsymbol{z})| \leq \frac{\varepsilon_1}{\Delta_v}|z_e^p| + \varepsilon_2|\tilde{\alpha}_c|, \quad |\bar{d}_2(t,\boldsymbol{z})| \leq \kappa_v |z_e^p| \tag{A.6}$$

for $\varepsilon_1 = 0.73$ and $\varepsilon_2 = 1.22$. This holds for all values of z_e^p and $\tilde{\alpha}_c$ but a less conservative stability result is obtained if the parameter projection algorithm (34) is applied. If $|\alpha_c| \leq M_\theta$ and $|\hat{\alpha}_c| \leq M_{\hat{\theta}}$ where $M_{\hat{\theta}} = M_\theta + \epsilon$ and $\epsilon > 0$ is a small constant, it follows that $|\tilde{\alpha}_c| = |\alpha_c - \hat{\alpha}_c| \leq 2M_\theta + \epsilon$. This suggests that smaller values than 0.73 and 1.22 can be used for ε_1 and ε_2 by specifying M_θ. For instance, we can limit the parameter estimation error $|\tilde{\alpha}_c|$ to 10.0 degrees by choosing $M_\theta = 0.087$ (4.98 degrees) and $\epsilon = 0.0001$. This gives $\varepsilon_1 = 0.088$ and $\varepsilon_2 = 0.006$.

Furthermore, consider the Lyapunov function candidate $V(\boldsymbol{z}) = \boldsymbol{z}^{\top}\boldsymbol{P}_v\boldsymbol{z}$ where $\boldsymbol{P}_v = \boldsymbol{P}_v^{\top} > 0$. Consequently,

$$\begin{aligned} \dot{V}(\boldsymbol{z}) &= U_v \Omega_v(\boldsymbol{z}) \Big(\boldsymbol{z}^{\top}(\boldsymbol{P}_v\boldsymbol{A}_v + \boldsymbol{A}_v^{\top}\boldsymbol{P}_v)\boldsymbol{z} \\ &\quad + 2\bar{\boldsymbol{d}}(t,\boldsymbol{z})^{\top}\boldsymbol{P}_v\boldsymbol{z} + 2\kappa_v \frac{U_v^{\min}}{U_c}[0,\ Q]\boldsymbol{P}_v\boldsymbol{z} \Big) \\ &\leq U_v^{\min}\Omega_v(\boldsymbol{z}) \Big(-z^{\top}\boldsymbol{Q}_v\boldsymbol{z} \\ &\quad + 2\frac{U_v^{\max}}{U_v^{\min}}\bar{\boldsymbol{d}}(t,\boldsymbol{z})^{\top}\boldsymbol{P}_v\boldsymbol{z} + 2\kappa_v[0,\ Q]\boldsymbol{P}_v\boldsymbol{z} \Big) \end{aligned} \tag{A.7}$$

where it has been exploited that the matrix $\boldsymbol{A}_v$ is Hurwitz for all $\gamma_v > 0$ and $\Delta_v > 0$, and therefore we can choose $\boldsymbol{Q}_v = \mathrm{diag}\{q_1, q_2\} > 0$ with $\boldsymbol{P}_v$ satisfying the Lyapunov equation $\boldsymbol{P}_v\boldsymbol{A}_v + \boldsymbol{A}_v^{\top}\boldsymbol{P}_v = -\boldsymbol{Q}_v$. This yields

$$\boldsymbol{P}_v = \frac{1}{2\kappa_v}\begin{bmatrix} (q_2 + q_1\kappa_v)\Delta_v & q_2 \\ q_2 & q_1\kappa_v^2\Delta_v + q_2\kappa_v\Delta_v + \frac{q_2}{\Delta_v} \end{bmatrix} \tag{A.8}$$

The maximum eigenvalue $p_{\max} = \lambda_{\max}(\boldsymbol{P}_v)$ is

$$p_{\max} = \frac{1}{2}\left(p_{11} + p_{22} + \sqrt{p_{11}^2 - 2p_{11}p_{22} + p_{22}^2 + 4p_{12}^2} \right) \tag{A.9}$$

Since $\|\boldsymbol{x}\|_2 \leq \|\boldsymbol{x}\|_1$ for all $\boldsymbol{x} \in \mathbb{R}^2$ and $\|\boldsymbol{x}\|_1 = |x_1| + |x_2|$, it follows that $\|\bar{\boldsymbol{d}}(t,\boldsymbol{z})\|_2 \leq |\bar{d}_1(t,\boldsymbol{z})| + |\bar{d}_2(t,\boldsymbol{z})|$ and $\|\boldsymbol{z}\|_2 \leq |z_e^p| + |\tilde{\alpha}_c|$. Hence,

$$\begin{aligned} 2\frac{U_v^{\max}}{U_v^{\min}}\|\bar{\boldsymbol{d}}(t,\boldsymbol{z})^{\top}\boldsymbol{P}_v\boldsymbol{z}\|_2 &\leq 2\frac{U_v^{\max}}{U_v^{\min}}\|\bar{\boldsymbol{d}}(t,\boldsymbol{z})\|_2\, \|\boldsymbol{P}_v\|_2\, \|\boldsymbol{z}\|_2 \\ &\leq 2\frac{U_v^{\max}}{U_v^{\min}} p_{\max}\left(\left(\frac{\varepsilon_1}{\Delta_v} + \kappa_v\right)|z_e^p| + \varepsilon_2|\tilde{\alpha}_c| \right)\left(|z_e^p| + |\tilde{\alpha}_c| \right) \\ &\leq 2\frac{U_v^{\max}}{U_v^{\min}} p_{\max}\left(\left(\frac{\varepsilon_1}{\Delta_v} + \kappa_v\right)|z_e^p|^2 + \varepsilon_2|\tilde{\alpha}_c|^2 \right. \\ &\quad \left. + \left(\frac{\varepsilon_1}{\Delta_v} + \varepsilon_2 + \kappa_v\right)|z_e^p||\tilde{\alpha}_c| \right) \end{aligned} \tag{A.10}$$

The product, $2\kappa_v\,[0,\ Q]\boldsymbol{P}_v\boldsymbol{z}$, due to projection, satisfies

$$\begin{aligned} 2\kappa_v\|\,[0,\ Q]\,\boldsymbol{P}_v\boldsymbol{z}\|_2 &= 2\kappa_v|p_{12}Qz_e^p + p_{22}Q\tilde{\alpha}_c| \\ &\leq q_2|z_e^p|^2 \end{aligned} \tag{A.11}$$

since $p_{12} = q_2/(2\kappa_v)$, $p_{22} > 0$, and $Q\tilde{\alpha}_c \leq 0$. Consequently, it follows from (A.7) that

$$\dot{V}(\boldsymbol{z}) \leq -U_v^{\min}\Omega_v(\boldsymbol{z})\boldsymbol{z}^{\top}\boldsymbol{Q}_v^*\boldsymbol{z} \tag{A.12}$$

$$\boldsymbol{Q}_v^* = \begin{bmatrix} q_1 - q_2 - 2p_{\max}(\frac{\varepsilon_1}{\Delta_v} + \kappa_v) & -c_q(\frac{\varepsilon_1}{\Delta_v} + \varepsilon_2 + \kappa_v) \\ -c_q(\frac{\varepsilon_1}{\Delta_v} + \varepsilon_2 + \kappa_v) & q_2 - 2p_{\max}\varepsilon_2 \end{bmatrix} \tag{A.13}$$

where $c_q = p_{\max}U_v^{\max}/U_v^{\min}$. Hence, we can choose q_1, q_2 and κ_v such that $\boldsymbol{Q}_v^* > 0$, and there exists a minimum eigenvalue $q_{\min} = \lambda_{\min}(\boldsymbol{Q}_v^*) > 0$ such that

$$\dot{V}(\boldsymbol{z}) \leq -U_v^{\min}q_{\min}\Omega_v(\boldsymbol{z})\boldsymbol{z}^{\top}\boldsymbol{z} \tag{A.14}$$

For instance, $\varepsilon_1 = 0.088$, $\varepsilon_2 = 0.006$, $\Delta_v = U_v^{\min} = 0.500$, $\gamma_v = 0.090$, $\kappa_v = 0.180$, $\boldsymbol{Q}_v = \mathrm{diag}\{0.1, 0.0036\}$, and $U_v^{\max} = 0.545$ give two positive definite matrices

$$\boldsymbol{P}_v = \begin{bmatrix} 0.0293 & 0.0085 \\ 0.0085 & 0.023 \end{bmatrix}, \quad \boldsymbol{Q}_v^* = \begin{bmatrix} 0.0720 & -0.0138 \\ -0.0138 & 0.0027 \end{bmatrix}$$

for which $p_{\max} = 0.035$ and $q_{\min} = 1.19e^{-6}$. Computation of the $\boldsymbol{P}_v$ and $\boldsymbol{Q}_v$ matrices depend on $U_v^{\min}$, $U_v^{\max}$, the maximum parameter estimation error, etc. It is well known that the Lyapunov stability results are conservative but the numerical example shows that solutions can be found by specifying realistic values. For each $r > 0$ and all $\|\boldsymbol{z}(t)\|_2 \leq r$, we have that

$$\Omega_v(\boldsymbol{z}) \geq \frac{\Delta_v}{\sqrt{\Delta_v^2 + r^2}} := c(r) \tag{A.15}$$

$$\dot{V}(\boldsymbol{z}) \leq -U_v^{\min}q_{\min}c(r)\boldsymbol{z}^{\top}\boldsymbol{z} \leq -2U_v^{\min}\frac{q_{\min}}{p_{\max}}c(r)V(\boldsymbol{z}) \tag{A.16}$$

Since $V(\boldsymbol{z}) > 0$ and $\dot{V}(\boldsymbol{z}) < 0$ whenever $\boldsymbol{z} \neq \boldsymbol{0}$, it follows from Khalil (2002, Theorem 4.8) that the origin $\boldsymbol{z} = \boldsymbol{0}$ is uniformly stable and $\|\boldsymbol{z}(t)\|_2 \leq \|\boldsymbol{z}(t_0)\|_2, \forall t \geq t_0$. The above holds for all trajectories generated by the initial conditions $\boldsymbol{z}(t_0)$. Hence, we can invoke the comparison lemma (Khalil, 2002, Lemma 3.4), by noticing that the system $\dot{\chi} = -2U_v^{\min}(q_{\min}/p_{\max})c(r)\chi$ has the solution $\chi(t) = e^{-2U_v^{\min}(q_{\min}/p_{\max})c(r)(t-t_0)}\chi(t_0)$, which implies that $\dot{w}(t) \leq e^{-2U_v^{\min}(q_{\min}/p_{\max})c(r)(t-t_0)}w(t_0)$ for $w(t) = V(\boldsymbol{z})$. Consequently,

$$\|\boldsymbol{z}(t)\|_2 \leq \sqrt{\frac{p_{\max}}{p_{\min}}}e^{-U_v^{\min}\frac{q_{\min}}{p_{\max}}c(r)(t-t_0)}\|\boldsymbol{z}(t_0)\|_2 \tag{A.17}$$

for all $t \geq t_0$, $\|\boldsymbol{z}(t_0)\|_2 \leq r$ and any $r > 0$. This allows us to conclude that the equilibrium point $\boldsymbol{z} = \boldsymbol{0}$ is USGES (Loria & Panteley, 2004, Definition 2.7).

Appendix B. Proof of Lemma 2

In the horizontal-plane (42) can be expressed by $\dot{\boldsymbol{y}} = U_h\Omega_h(\boldsymbol{y})\boldsymbol{A}_h\boldsymbol{y}$ where $\boldsymbol{y} = [y_1,\ y_2]^{\top} := [y_e^p,\ \tilde{\beta}_c]^{\top}$, and

$$\boldsymbol{A}_h = \begin{bmatrix} -1/\Delta_h & 1 \\ -\kappa_h & 0 \end{bmatrix}, \quad \Omega_h(\boldsymbol{y}) = \frac{\Delta_h}{\sqrt{\Delta_h^2 + (y_e^p)^2}} \tag{B.1}$$

Hence, Lemma 1 guarantees that $\boldsymbol{y} = \boldsymbol{0}$ is USGES.

Appendix C. Proof of Theorem 1

The systems Σ_1 and Σ_2 corresponding to (41)–(42) forms a cascade. Note also that the perturbation term $g(t, y_e^p, \tilde{\beta}_c)$ defined in (38) is bounded and that

$$g(t, 0, 0) = U_h \sin(\pi_v) \left(1 - \frac{1}{\sqrt{1 + \tan^2(\beta_c)}} \right) \tag{C.1}$$

Lemma 2 guarantees that the Σ_2 states y_e^p and $\tilde{\beta}_c$ converge exponentially to zero. From Khalil (2002, Lemma 9.1), one can also conclude that if $\pi_v = 0$ (constant depth) or $\beta_c = 0$ (zero sideslip), the origin of Σ_1 is USGES since the perturbation vanishes at zero and there is no growth by the states z_e^p and $\tilde{\alpha}_c$. For the case that $\beta_c \neq 0$ but constant (Assumption 1), $\pi_v \neq 0$, and u is time varying with $0 < u_{\min} \leq u \leq u_{\max}$, one can conclude using Khalil (2002, Lemma 9.6, Case 2), that the solution of the perturbed system Σ_1 is uniform ultimate bounded since $g(t, y_e^p, \tilde{\beta}_c)$ is bounded. Moreover, notice that origin of the Σ_1 subsystem will be shifted. The steady-state solution $\dot{z}_e^p = \dot{\tilde{\alpha}}_c = 0$ of (41) gives

$$(z_e^p)^{ss} \equiv 0, \quad \tilde{\alpha}_c^{ss} \equiv -\sin^{-1}(g(t, 0, 0)/U_v) \tag{C.2}$$

Thus if the speed autopilot keeps u constant during path following, then U_v given by (12) is constant. Hence, it follows that z_e^p converges to zero but the estimate of α_c will be shifted with a constant value, which is very small for most vehicles. The bias free estimate is given by $\hat{\alpha}_c^* = \hat{\alpha}_c - \sin^{-1}(g(t, 0, 0)/U_v)$.

References

Aguiar, A. P., Hespanha, J. P., & Kokotović, P. (2008). Performance limitations in reference-tracking and path-following for nonlinear systems. *Automatica*, *44*(3), 598–610.

Beard, R. W., & McLain, T. W. (2012). *Small unmanned aircraft. Theory and practice*. Princeton Univ. Press.

Børhaug, E., Pavlov, A., & Pettersen, K. Y. (2008). Integral LOS control for path following of underactuated marine surface vessels in the presence of constant ocean currents. In *IEEE conference on decision and control* (pp. 4984–4991). Cancun, Mexico.

Breivik, M., & Fossen, T. I. (2005). Principles of guidance-based path following in 2-D and 3-d. In *IEEE conference on decision and control and the European control conference* (pp. 627–634). Seville, Spain.

Breivik, M., & Fossen, T. I. (2009). Guidance laws for autonomous underwater vehicles. In A. V. Inzartsev (Ed.), *Intelligent underwater vehicles* (pp. 51–76). Vienna, Austria: I-Tech Education and Publishing, Ch. 4.

Caharija, W. (2014). *Integral line-of-sight guidance and control of underactuated marine vehicles* (Ph.D. thesis), Trondheim, Norway: Norwegian University of Science and Technology, Dept. of Eng. Cybernetics.

Caharija, W., Pettersen, K. Y., Bibuli, M., Calado, P., Zereik, E., Braga, J., Gravdahl, J. T., Sørensen, A. J., Milovanovic, M., & Bruzzone, G. (2016). Integral line-of-sight guidance and control of underactuated marine vehicles: Theory, simulations, and experiments. *IEEE Transactions on Control Systems Technology*, *24*(5), 1623–1642.

Caharija, W., Pettersen, K. Y., Calado, P., & Braga, J. (2015). A Comparison between the ILOS guidance and the vector field guidance. In *IFAC proc.: vol. 48, IFAC conf. on manoeuvering and control of marine craft* (pp. 89–94). (16).

Fossen, T. I. (2021). *Handbook of marine craft hydrodynamics and motion control*. Chichester, UK: Wiley.

Fossen, T. I. (2023a). An adaptive line-of-sight (ALOS) guidance law for path following of aircraft and marine craft. *IEEE Transactions on Control Systems Technology*, *31*(6), 2887–2894.

Fossen, T. I. (2023b). An amplitude-phase representation of the North-East-Down kinematic differential equations. *IEEE Access*, *11*, 12587–12593.

Fossen, T. I., Breivik, M., & Skjetne, R. (2003). Line-of-sight path following of underactuated marine craft. In *IFAC proc.: vol. 36, IFAC conf. on maneouvring and control of marine craft* (pp. 211–216). Girona, Spain: (21).

Fossen, T. I., & Lekkas, A. (2015). Direct and indirect adaptive integral line-of-sight path-following controllers for marine craft exposed to ocean currents. *International Journal of Adaptive Control and Signal Processing*, *31*(4), 445–463.

Fossen, T. I., & Perez, T. (2004). Marine systems simulator (MSS). https://github.com/cybergalactic/MSS.

Fossen, T. I., & Pettersen, K. Y. (2014). On uniform semiglobal exponential stability (USGES) of proportional line-of-sight guidance laws. *Automatica*, *50*, 2912–2917.

Fossen, T. I., Pettersen, K. Y., & Galeazzi, R. (2015). Line-of-sight path following for Dubins paths with adaptive sideslip compensation of drift forces. *IEEE Transactions on Control Systems Technology*, *23*(2), 820–827.

Healey, A. J., & Lienard, D. (1993). Multivariable sliding mode control for autonomous diving and steering of unmanned underwater vehicles. *IEEE Journal of Oceanic Engineering*, *18*(3), 327–339.

Ioannou, P. A., & Sun, J. (2012). *Robust adaptive control*. Mineola, New York: Dover Publications Inc..

Khalil, H. K. (2002). *Nonlinear systems*. Prentice-Hall.

Krstic, M., Kanellakopoulos, I., & Kokotovic, P. V. (1995). *Nonlinear and adaptive control design*. New York, NY: John Wiley & Sons, Inc..

Lekkas, A. M., & Fossen, T. I. (2012). A time-varying lookahead distance guidance law for path following. In *IFAC conf. on maneouvring and control of marine craft*. Arenzano, Italy: 19-21 September.

Lekkas, A. M., & Fossen, T. I. (2013). Line-of-sight guidance for path following of marine vehicles. In O. Gal (Ed.), *Advanced in marine robotics* (pp. 63–92). LAP LAMBERT Academic Publishing, Chapter 5.

Lekkas, A. M., & Fossen, T. I. (2014). Integral LOS path following for curved paths based on a monotone cubic Hermite spline parametrization. *IEEE Transactions on Control Systems Technology*, *22*(6), 2287–2301.

Liu, C., Sun, J., & Zou, Z. (2015). Integrated line of sight and model predictive control for path following and roll motion control using the rudder. *Journal of Ship Research*, *59*(2), 99–112.

Liu, L., Wang, D., & Peng, Z. (2017). ESO-based line-of-sight guidance law for path following of underactuated marine surface vehicles with exact sideslip compensation. *IEEE Journal of Oceanic Engineering*, *42*(2), 477–487.

Loria, A., & Panteley, E. (2004). Cascaded nonlinear time-varying systems: analysis and design. In F. Lamnabhi-Lagarrigue, A. Loria, & E. Panteley (Eds.), *Advanced topics in control systems theory* (pp. 23–64). London: Springer-Verlag, Ch. 2.

Nelson, D. R., Barber, D. B., McLain, T. W., & Beard, R. W. (2007). Vector field path following for miniature air vehicles. *IEEE Transactions on Robotics*, *23*(3), 519–529.

Oh, S.-R., & Sun, J. (2010). Path following of underactuated marine surface vessels using line-of-sight based model predictive control. *Ocean Engineering*, *37*(2), 289–295.

Park, S., Deyst, J., & How, J. P. (2007). Performance and Lyapunov stability of a nonlinear path following guidance method. *Journal of Guidance, Control, and Dynamics*, *30*(6), 1718–1728.

Pavlov, A., Nordahl, H., & Breivik, M. (2009). MPC-based optimal path following for underactuated vessels. In *IFAC conf. on maneouvring and control of marine craft* (pp. 340–345). Sao Paulo, Brazil.

Pelizer, G. V., da Silva, N. B. F., & Branco, K. R. L. J. (2017). Comparison of 3D path-following algorithms for unmanned aerial vehicles. In *Int. conference on unmanned aircraft syst.* (pp. 498–505). Miami, FL.

Pettersen, K. Y. (2017). Lyapunov sufficient conditions for uniform semiglobal exponential stability. *Automatica*, *78*, 97–102.

Pettersen, K. Y., & Lefeber, E. (2001). Waypoint tracking control of ships. In *IEEE conference on decision and control* (pp. 940–945). Orlando, FL.

Rout, R., & Subudhi, B. (2021). Design of line-of-sight guidance law and a constrained optimal controller for an autonomous underwater vehicle. *IEEE Transactions on Circuits and Systems II*, *68*(1), 416–420.

Siouris, G. M. (2010). *Missile guidance and control systems*. Springer.

Sujit, P. B., Saripalli, S., & Sousa, J. B. (2014). Unmanned aerial vehicle path following: A survey and analysis of algorithms for fixed-wing unmanned aerial vehicles. *IEEE Control Systems Magazine*, *34*(1), 42–59.

Yanushevsky, R. (2011). *Guidance of unmanned aerial vehicles*. CRC Press.

Thor I. Fossen is a professor of Guidance, Navigation, and Control (GNC) at the Department of Engineering Cybernetics, Norwegian University of Science and Technology (NTNU), Trondheim. He received an M.Sc. in Marine Technology in 1987 and a Ph.D. in Engineering Cybernetics in 1991. Besides cybernetics, Fossen's research fields are aerospace engineering and marine technology. This includes GNC systems for uncrewed vehicles (AUV, UAV, USV), robotics, vehicle dynamics, and inertial navigation systems. He has been a Fulbright scholar in flight control at the Department of Aeronautics and Astronautics of the University of Washington, Seattle. Fossen is the author of the Wiley textbook Handbook of Marine Craft Hydrodynamics and Motion Control (2021). He is one of the co-founders and former Vice President of R&D of the company Marine Cybernetics, which DNV acquired in 2012. He is also a co-founder of ScoutDI (2017), which develops drone-based systems for fully digitalized inspections of industrial confined spaces. The Institute of Electrical and Electronics Engineers elevated him to IEEE Fellow in 2016. He received the Automatica Prize Paper Award in 2002 and the Arch T. Colwell Merit Award in 2008 at the SAE World Congress. He was elected to the Norwegian Academy of Technological Sciences (1998) and the Norwegian Academy of Science and Letters (2022).

A. Pedro Aguiar received the Ph.D. in Electrical and Computer Engineering (ECE) from the Instituto Superior Técnico (IST), University of Lisbon, Portugal in 2002. He is currently a Full Professor with the ECE Department at the Faculty of Engineering, University of Porto (FEUP) and Director of ARISE - Advanced Production and Intelligent Systems Associate Laboratory. From 2002 to 2005, he was a post-doctoral researcher at the Center for Control, Dynamical-Systems, and Computation at the University of California, Santa Barbara (UCSB). From 2005 to 2012, he was a senior researcher with the Institute for Systems and Robotics at IST, and an invited professor with the ECE Department at IST, Lisbon. His research interests include modeling, control, navigation, and guidance of autonomous robotic vehicles, nonlinear control, switched and hybrid systems, tracking, path-following, performance limitations, nonlinear observers, the integration of machine vision with feedback control, networked control, and coordinated/cooperative control of multiple autonomous robotic vehicles.